International Journal of Basic and Applied Chemical Sciences ISSN: 2277-2073
Online, Open Access International Journal, Available at http://www.cibtech.org/jcs.htm
2022, Vol.12, pp.6-26/Shukla et al.
***Research Article** (Open Access)*

SYNTHESIS AND CHARACTERIZATION OF ISOTHIOCYANATO COMPLEXES OF DIOXOTUNGSTEN(VI) WITH SCHIFF BASE LIGANDS: SPECTROSCOPIC CHARACTERIZATION, DFT, ANTI-CORROSION ACTIVITY, AND ANTIBACTERIAL ACTIVITY

Satyendra Nath Shukla*, Pratiksha Gaur, Vijay Chakravarti, and Sanjay Singh Bagri
Coordination Chemistry Research Lab, Department of Chemistry,
Government Science College, Jabalpur (M.P.) 482001, India
**Author for Correspondence: sns1963_1@rediffmail.com*

ABSTRACT

Two Schiff base ligands 1-((E)-(p-nitro- phenyl)hydrazin)naphthalen-2-ol, (**L_1**) and 1-((E)-(p-phenyl)hydrazin)naphthalen-2-ol, (**L_2**) were synthesized by the condensation of the 2-hydroxy-1-naphthaldehyde with phenyl hydrazine/4-nitrophenylhydrazine.The tailored reaction of $(NH_4)_2[WO_2(NCS)_4]$ with Schiff base ligands in 1: 1 yielded two complexes $[WO_2(NCS)(H_2O)(L_1)]$, (1), and $[WO_2(NCS)(H_2O)(L_2)]$,(2) The structure of ligands and complexes has been discussed in the light of molar conductance, electronic spectra, FT-IR, ^{1}H-NMR, ^{13}C-NMR, and ESI-MS analysis. DFT was employed for the geometry optimization of ligands and complexes. The FT-IR data have suggested that ligand is coordinated with metal through azomethine-N and phenolic-O. Correlation coefficients value between 0.9977 - 0.9959 shows satisfactory agreement in the theoretical and experimental of ^{1}H-NMR and ^{13}C-NMR. Synthesized ligands and complexes were screened for anticorrosion activity. The antibacterial activity of ligands and complexes has also been assayed against *E. coli* and compared with standard drugs.

Keywords: *Dioxotungsten(VI) complex, DFT, Anticorrosion activity, Antibacterial activity*

INTRODUCTION

The chemistry of tungsten is multifaceted due to its many stable and accessible oxidation states. It is the only element of the third transition series whose presence even in trace amounts plays an important role in biological processes through various enzymatic reactions [1 - 3]. For some species presence of tungsten is essential for life, for some other species it is a facultative bioelements. Tungsten and its compounds are known to catalyze various chemical reactions. The increasing instances of multidrug, extended drug and pan-drug resistance among various pathogens pose a threat to global health [4]. Thus there is an urgent need for the development of new antibacterial agents. Schiff bases are an important class of ligands due to their extensive applications [5, 6]. In recent years, the synthesis of Schiff base derivative of transition metals is trending due to their role as catalysts in many reactions [7 - 9]. Very recently Schiff base derivatives derived from heterocyclic compounds have drawn attention due to their broad range of antibacterial activity [10 - 13]. In addition to this, some tungsten Schiff base complexes are known to exhibit anticorrosive properties. Thus, based on the above-cited literature we were inspired to synthesize some Schiff base ligands and their tungsten derivative and characterized them by spectroscopic techniques. Since DFT is a simulation technique to characterize the compounds theoretically, we used DFT for geometry optimization. In the present case, $Na_2WO_4.2H_2O$ was used as starting material to obtain $(NH_4)_2[WO_2(NCS)_4]$, a precursor to synthesize the present tungsten (VI) complexes.

The Scheme of reaction is as follows:

$Na_2WO_4.2H_2O + 2HCl \longrightarrow H_2WO_4 + 2NaCl + H_2O$

$H_2WO_4 + 4NH_4SCN \longrightarrow (NH_4)_2[WO_2(NCS)_4] + 2NH_4OH$

$[WO_2(NCS)_4]^{2-} + L_1H/L_2H \longrightarrow [WO_2(NCS)(H_2O)(L_1/L_2)]$

Where for L_1= 1-((E)-(*p*-nitro-phenyl)hydrazine)naphthalen-2-ol

L_2= 1-((E)-(*p*-phenyl)hydrazine)naphthalen-2-ol

Figure 1: Scheme of reaction

MATERIALS AND METHODS

Sodium tungstate dehydrates (99%), (Merck Life Science India), and ammonium thiocyanate (Research lab India), were used as received. 2-Hydroxy-1-naphthaldehyde, phenylhydrazine, and nitrophenyl hydrazine were purchased from Sigma Aldrich USA. Analytical reagent grade methyl alcohol, ethyl alcohol, acetonitrile, chloroform, acetone, dimethylformamide, dimethylsulphoxide, and other solvents were used. Electronic absorption spectra were recorded with EI- 2371 UV-Visible double-beam spectrophotometer equipped with a PC. Conductivity measurements were carried out at 25 °C on the EI-181 digital conductivity bridge with a dipping-type cell in DMSO. FT-IR spectra were recorded in KBr pellets on a Shimadzu-8400 PC FT-IR spectrophotometer in the region of 4000-400 $cm^{-1}$and the spectra were drawn in IR Solution software with no. of scan 25 and resolution of 4 cm^{-1}. ^{1}H-NMR spectra were recorded on a Jeol spectrometer at 400 MHz. The ^{13}C-NMR spectrum was recorded in Bruker Avance-400 (FT-NMR) using Topspin 2.1 software. The ESI-MS spectra were recorded on Agilent 6520 (QTOF) mass spectrophotometer. The metal contents were analyzed gravimetrically by the literature procedure [14].

Synthesis of ligands

Synthesis of Schiff base ligand 1-((E)-(p-nitro-phenyl)hydrazin)naphthalen-2-ol; L_1

The starting material 2-hydroxy-1-naphthaldehyde (0.860 g, 0.005 mol) was dissolved in 20 mL hot ethanol and added to the solution of 4-nitrophenyl hydrazine (0.765 g, 0.005 mol) dissolved in 20 mL ethanol. The resulting reaction mixture was initially stirred for 1 h at room temperature and thereafter refluxed for 18 h under an inert atmosphere. On cooling, a red-coloured precipitate was obtained which was filtered off, washed with H_2O, ethanol, and recrystallized with hot methanol, and dried under vacuum. Colour = Red, Yield: 1.231 g (59.04 %); m. p. = 209 °C. Anal. Found: C, 66.34; H, 4.26; N, 13.57; $C_{17}H_{13}N_3O_3$ (M_τ = 307.3) Require: C, 66.40; H, 4.31; N, 13.62. UV–visible (λ_{max} in nm (ε in $mol^{-1}L\ cm^{-1}$) in DMSO 10^{-4} M: 220(2756), 250(2179), 270(2194), 290(2000). Selected infrared absorption (KBr, cm^{-1}): ν(O-H), 3492; ν(N-H), 3365; ν(-CH=N), 1622; ν(NO_2), 1284; ν(C-O), 1273. ^{1}H-NMR (DMSO-d_6, 400 MHz) spectra (δ value in ppm): δ(O-H), 15.321(s, 1H); δ(N-H), 10.812(s, 1H); δ(CH=N), 8.891(s, 1H); $\delta(Ar\text{-}H)_{Phenolic}$8.535(d, *J* = 11.2, 1H) 8.324(dd, *J* = 9.6, 3.6 Hz, 1H), 8.125(d, *J* = 12.0 Hz, 1H), 7.962(t, *J* = 12.8 Hz, 1H), 7.811(dd, *J* = 8.8, 4.4 Hz, 1H), 7.392(t, *J* = 5.6, 4.8 Hz, 1H); $\delta(Ar\text{-}H)_{Substituted}$,7.233(d, *J* = 12.0,1H), 6.995(d, *J* = 12.4,1H), 6.796(d, *J* =12.4, 1H), 6.604(d, *J* = 6.8, 1H); ^{13}C-NMR spectra (δ value in ppm): (OH), 171.89; $\delta(HC{=}N)_{amine,}$ 163.84; $\delta(Ar\text{-}C)_{Phenolic}$156.47, 155.63, 153.17, 144.72,138.29, 133.01, 129.09, 128.76, 128.38 $\delta(Ar\text{-}C)_{Substituted,}$ 126.85, 124.15, 124.02, 122.17, 122.07, 121.12 ESI-Mass spectra *m/z*:$[C_{11}H_9N_2O+H^+]^+$ = 186.2, $[C_{17}H_{13}N_2O+H^+]^+$ = 262.3, $[C_{17}H_{12}N_3O_2+H^+]^+$ = 291.0, $[C_{17}H_{13}N_3O_3+H^+]^+$ = 308.3,M_τ = 307.3.

Synthesis Of Schiff Base Ligand 1-((E)-(p- phenyl)hydrazin)naphthalen-2-ol; L_2

The starting material 2-hydroxy-1-naphthaldehyde (0.860 g, 0.005 mol) was dissolved in 20 mL hot ethanol and added to the solution of phenylhydrazine (0.523 mL, 0.005 mol) dissolved in 20 mL ethanol. The resulting reaction mixture was initially stirred for 2 h at room temperature and thereafter refluxed for 20 h under an inert atmosphere. On cooling, a yellow precipitate was obtained which was filtered off, washed with H_2O, ethanol and recrystallized with hot methanol, and dried under vacuum. Colour = Shining yellow, Yield: 1.081 g (49.03 %); m. p. = 201 °C. Anal. Found: C, 77.74; H, 5.28; N, 10.55; $C_{17}H_{14}N_2O$ (M_τ = 262.373) Require: C, 77.79; H, 5.33; N, 10.61. Electronic spectra (λ_{max} in nm (ε in ($mol^{-1}L\ cm^{-1}$)) in UV–visible (DMSO 10^{-4} M): 210(1138), 240(2754), 260(3505), 280(3702). Selected infrared

absorption (KBr, cm^{-1}): ν(O-H) 3490, ν(C-N) 3361, ν(-CH=N) 1620, ν(C-O) 1281. ^{1}H-NMR (DMSO-d_6, 400 MHz) spectra (δ value in ppm): δ(OH), 15.318(s, 1H); δ(N-H), 10.819(s, 1H); δ(CH=N), 8.848(s, 1H); δ(Ar-H)$_{Phenolic}$8.541(d, *J* = 11.5, 1H), 8.357(dd, *J* = 9.3, 3.7, 1H), d 8.117(d, *J* = 12.2, 1H), 7.971(t, *J* = 12.5, 1H), 7.823(dd, *J* = 8.7, 4.5, 1H), 7.381(t, *J* = 5.3, 4.6, 1H).δ(Ar-H)$_{Substituted}$7.227(d, *J* = 12.2,1H), 6.982 (d, *J* = 12.5,1H), 6.789(d, *J* =12.1,1H), 6.613(d, *J* = 6.9,1H), 6.546(m, 1H).^{13}C-NMR spectra (δ value in ppm): δ(C-OH), 170.82; δ(C=N), 162.77; δ(C-N) 156.40; δ(Ar-C)$_{Phenolic}$ 154.61, 151.11, 140.71, 133.25, 132.96, 128.88, 128.72, 128.31, δ(Ar-C)$_{Substituted}$124.10, 124.08, 122.07, 122.03, 121.08; ppm ESI-Mass spectra *m/z* $[C_{10}H_7 + H^+]^+$= 127.0, $[C_{10}H_7O+H^+]^+$ = 143.3, $[C_{11}H_9N_2+H^+]^+$ = 169.0, $[C_{11}H_8NO+H^+]^+$ = 170.2, $[C_{17}H_{13}N_2+H^+]^+$ = 245.0, $[C_{17}H_{14}N_2O+H^+]^+$ = 263.2, M_τ. = 262.2.

Synthesis of complexes

The precursor dioxotungsten(VI) isothiocyanato complex was prepared by following a procedure reported earlier [15]. The sodium tungstate dihydrate (0.60 g, 0,0018 mmo1) and ammonium thiocyanate (~ 19 mmo1, 1.45 g) in excess, were dissolved in 15 ml water and 3.75 ml of 11 M HCl. to yield a yellow solution of tetrathiocyanato dioxotungsstate (VI)anion. To this solution of precursor, **L_1** (0.552 g, 0.0018 mol)/ **L_2** (0.472 g, 0.0018 mol) dissolved in 15 mL hot ethanol was added and stirred for 40 min. The reaction mixture was stirred for 2 h in an ice bath. On slow evaporation a dark red/dark green solid was obtained which was filtered, washed with water, diethyl ether, and recrystallized from 1: 2: 3, acetonitrile: acetone: chloroform (v/v/v) solvent mixture to yield a dark red/dark green crystalline solid, which was dried in a desiccator over anhydrous calcium chloride under vacuum.

[WO_2(NCS)(H_2O)(L_1)],(1);

Analytical data: Colour = Dark red, Yield: 0.782 g (68.21 %); m. p. > 243-246°C; Anal. Found: C, 36.04; H, 2.30; N, 9.32; S, 5.20; W, 30.53; Calcd for $C_{18}H_{14}N_4O_6SW$ (M_τ = 598.23): Require: C, 36.14; H, 2.36; N, 9.37; S, 5.36; W, 30.73. Molar conductance Λ_m at 25°C (Ω^{-1} cm^2 mol^{-1}): 1.11 in DMSO. Electronic spectra (λ_{max} in nm (ε in (L mol^{-1} cm^{-1})) in DMSO: 270(1236), 290(1017), 310(1810). Selected infrared absorption (KBr, cm^{-1}): ν(NH), 3356; ν(C=N), 2069; ν(CH=N), 1617;ν (NO_2), 1281; ν(C-O), 1270;ν(WO_2)asym, 958; ν(WO_2)sym, 869; ν(C=S), 784; ν(W-O), 560; ν(NCS+ M-N), 473. ^{1}H-NMR (DMSO-d_6, 400 MHz) spectra (δ value in ppm): δ(NH), 10.820 (s, 1H); δ(CH=N), 8.928 (s, 1H); δ(Ar-H)$_{phenolic}$ 7.517(m, 3H), 7.306(m, 3H), δ(Ar-H)$_{Substituted}$, 8.461(d, *J* = 11.2, 1H), 7.891(d, *J* = 12.4, 1H), 7.766(d, *J* = 12.0, 1H), 6.956(d, *J* = 12.4, 1H), ^{13}C-NMR spectra (δ value in ppm): δ (C-OH), 166.28; δ(HC=N), 158.66; δ(Ar-C)$_{Phenolic}$ 157.51, 143.00, 138.79, 136.28, 132.33, 130.13,129.95, 129.67, 127.51; δ(Ar-C)$_{Substituted,}$ 126.84, 126.28, 125.90, 122.15, 122.01. ESI-Mass spectra, *m/z*: $[CH_2NO_3SW+H^+]^+$ = 292.064, $[C_{17}H_{12}N_3O_3+H^+]^+$ = 307.188, $[C_{18}H_{14}N_3O_4SW+H^+]^+$ = 553.023, $[C_{18}H_{14}N_4O_6SW +H^+]^+$ = 599.23, M_τ = 598.23.

[WO_2(NCS)(H_2O)(L_2)], (2)

Analytical data: Colour = Dark green; Yield: 0.252 g (42.44 %); m. p. = 211-213°C; Anal. Found C, 38.46; H, 2.21; N, 9.44; S, 10.81; W, 30.99; Calcd for $C_{18}H_{15}N_3O_4SW$ (M_τ = 553.345): Found C, 39.08; H, 2.73; N, 7.60; S, 5.80; W, 33.23. Molar conductance Λ_m at 25°C (Ω^{-1} cm^2 Mo^{-1}): 1.20 in DMSO. Electronic spectra (λ_{max} in nm (ε in (Mo^{-1} L cm^{-1})) in DMSO: 260(1346), 290(978), 320(768). Selected infrared absorption (KBr, cm^{-1}): ν(NH), 3357; ν(C=N), 2066; ν(CH=N), 1616; ν(C-O), 1274;ν (WO_2)$_{asym}$, 954; ν(WO_2)$_{sym}$, 866; ν(C=S), 783; ν(W-O), 557; ν(NCS+ M-N), 470.^{1}H-NMR (DMSO-d_6, 400 MHz) spectra (δ value in ppm): δ(N-H), 10.823 (s, 1H); δ(CH=N), 8.934 (s, 1H); δ(Ar-H)$_{Phenolic}$ 7.615(m , 3H), 7.268(m, 3H), δ(Ar-H)$_{Substituted}$, 8.356 (d, *J* =11.2, 1H), 7.771(d, *J* =12.4, 1H), 7.675(d, *J* =12.0, 1H), 6.827(d, *J* =12.4, 1H). ^{13}C-NMR spectra (δ value in ppm): (Ar-C-OH), 166.56; δ(HC=N), 158.53; δ(Ar-C)$_{Phenolic}$ 157.42, 144.55, 139.19, 137.51, 134.51, 130.74, 129.78, 127.06, 125.35, δ(Ar-C)$_{Substituted,}$ 126.17, 126.07, 125.83, 122.56, 120.24 ppm. ESI-Mass spectra, *m/z*: $[C_{17}H_{13}N_2O+H^+]^+$= 262.080, $[C_{12}H_{10}N_3O_4SW +H^+]^+$= 476.99, $[C_{18}H_{15}N_3O_4SW +H^+]^+$= 554.3, Mτ = 553.23

DFT Study

The theoretical calculation manifested by Gaussian 09 software package was performed to optimize the geometry of compounds[16]. To attain insight into the molecular structure, density functional theory calculations were carried out to optimize the structure of ligands and complexes **1-2**. Geometries of

ligands were optimized by the DFT method of B3LYP which is the hybrid of Becke's three-parameter exchange functional with the Lee–Yang–Parr correlation functional [17]. The electronic properties, such as the energy of HOMO and LUMO orbitals were calculated using TD-SCF, DFT/6-31G at the B3LYP level of theory based on the optimized structure in the gas phase. The parameters used to describe the reactivity and stability of a Molecule such as ΔE, Mulliken electronegativity (**χ**), dipole moment, chemical potential (**μ**), global hardness (**η**), global softness (**S**), global electrophilicity (**ω**), absolute softness (**σ**) and electronic charge ($\mathbf{\Delta}N_{max}$) have been calculated. The ^{1}H-NMR and ^{13}C-NMR chemical shifts of the Molecule were calculated by the gauge-independent atomic orbital (GIAO) method and compared with experimental results.

Anticorrosion activity

The anticorrosion activity of ligands and complexes was done by the weight loss measurement method [18]. The coupons of mild steel cut (30 x 40 x 0.5 mm) were mechanically abraded with 320, 400, 600, 800, 1000, 1500, and 2000 grades of emery papers. It was then degreased with acetone washed with double distilled water and dried in air and immersed in triplicates in 50 mL of 1 M HCl solution a corrosive medium prepared from analytical grade HCl. A 50 ppm solution of ligands and complex 1-2 in 5 mL DMSO were added to the electrolyte at room temperature. The corroded/inhibited specimens were taken out from the electrolyte washed and rinsed thoroughly several times with distilled water, cleaned using acetone, dried, and reweighed on a digital balance with a sensitivity of 0.001 g after every 24, 48, and 72 h. The weight loss was calculated as the difference in weight of the specimen before and after immersion in corrosive media. The corrosion rate (**CR**) in mg cm^{-2} h^{-1} and corrosion inhibition efficiency (**η**) in % is calculated using an equation [19, 20].

$$CR = \frac{\Delta W}{a \times t}$$

$$\eta\ \% = \frac{CR^{\circ} - CR}{CR^{\circ}} \times 100$$

Where ΔW is average weight loss, a is the total area of the specimen and t is the immersion time, η is inhibition efficiency, CR° and CR are the corrosion rate of mild steel specimens in the absence and presence of inhibitor respectively.

Antibacterial activity

The agar well method was used for the screening of *in vitro* antibacterial activity [21, 22]. The antibacterial screening was performed against the gram-negative bacteria *Escherichia coli* (ATCC 2256). Chloramphenicol was used as a standard antibacterial drug. A hot nutrient agar solution (20 mL) was poured into the sterilized petri dishes and allowed to attain room temperature. The seed layer medium was melted and cooled to 45 ºC with gentle shaking. The previously grown subculture of bacteria was added to the seed layer medium aseptically and mixed well. It was immediately dried into the petri plate and allowed to attain room temperature. Then wells were made with a sterile cork borer and in these wells, 0.01-100 μ_g/mL of compound solution was added and the plates were allowed to cool for 1 h to facilitate the diffusion. The plates were incubated at 37 ºC for 48 h. At the end of the incubation period, the inhibition zone around the wells was measured. DMSO was used as a negative control under the same conditions for each organism. Finally, the petriplates were sealed by the parafilm and were kept in the incubator at 37 °C for 72 h. At the end of the incubation period, the inhibition zone around the wells was measured.

RESULTS AND DISCUSSION

Quantum chemical study

To attain an insight into the Molecular structure, density functional theory calculations were carried out to optimize the structure of $\mathbf{L_1}$, $\mathbf{L_2}$, and complex **1-2**. The elucidated quantum chemical parameters are shown in **Table 1**. The negative values of both E_{LUMO} and E_{HOMO} were indicative of the stability of synthesized ligands and complexes. The energy gap (ΔE) value of the ligand is high which indicates its high stability, hard nature, less reactivity, and flexibility in donating electrons from donor atom to metal.

The HOMO is the outermost filled orbital that behaves as an electron donor and is directly related to ionization potential, while LUMO act as an electron acceptor, greater in energy and related to electron affinity [23]. Since the energy gap, ΔE for compounds lies between 3.394 - 1.38 eV, which indicates that the samples can behave as semiconductors. However, with the energy gap, we are mainly concerned with the reactivity of the molecules. The theoretical chemical shift values were calculated by the GAIO method using TMS HF/6-31G(d)GIAO and TMS B3LYP/6-311+G(2d,p)GIAO level of theory. The predicted chemical shift values were in good agreement with experimental values.

Table1. The calculated quantum chemical parameters of ligands and complexes

Ligand / Complex	HOMO	LUMO	ΔE	Mulliken electronegativity, χ	Global Hardness	Absolute softness, σ	Chemical Potential, μ	Global Softness, S	Global Electrophilicity, ω	Electronic Charge, ΔN	Dipole Moment, μ	E(TD-HF/TD-KS)
L_1	-3.635	-2.255	1.38	2.945	0.695	1.4492754	-2.945	0.7246377	6.2848007	4.2681159	4.609	-1196.01
L_2	-8.646	-5.252	3.394	6.949	1.697	0.5892752	-6.949	0.2946377	14.227637	4.0948733	10.68	-1406.73
Complex**1**	-8.824	-5.921	2.903	7.3725	1.4515	0.688942	-7.3725	0.344471	18.72331	5.079228	9.965	-3062.18
Complex**2**	-4.93	-1.879	3.051	3.4045	1.5255	0.655523	-3.4045	0.327761	3.798958	2.231727	6.074	-1640.02

Mulliken atomic charge analysis

The Mulliken population analyses of $\mathbf{L_1}$ and complexes were done to calculate net atomic charges in ligands and complexes[24]. Atomic charge analysis has an important role in the molecular system because it affects dipole moment, molecular polarizability, and other properties of the molecule. The result shows that in $\mathbf{L_1}$ the highest positive charge exists on H23 (+0.3611) because it is attached to the electronegative oxygen atom. The highly shielded electronegative atom O17 possesses a charge of -0.6104. However, in complexes **1-2** the highest positive charge was observed at the metal center. The other electronegative atoms such as phenolic oxygen and azomethine nitrogen contain a negative Mulliken charge because of the high electron density on these atoms. The N atoms of the anchored heterocyclic ring are electron-rich and possess a negative Mulliken charge. Electropositive carbon and electronegative oxygen/nitrogen exhibit higher Mulliken charge probably due to the occurrence of back bonding. These results are consistent with the Molecular electrostatic potential (MEP) map. Mulliken atomic charge plot and pattern of $\mathbf{L_1}$ and complex **1** are displayed in **Figures 2 (a)** and **(d).**

Molecular electrostatic potential analysis (MEP) and contour map

The Molecular electrostatic potential (MEP) is an important parameter to explore the different sites for electrophilic/nucleophilic reactions and hydrogen-bonding interactions. The Molecular electrostatic potential, (r), at a given point r (x, y, z) in the vicinity of a Molecule is defined in terms of the interaction energy between the electrical charge generated from the Molecule electrons and nuclei. It also provides a visual method to understand the reactivity of the Molecules and is widely used for predicting the sites that are susceptible to nucleophilic and electrophilic attacks on Molecular species. To predict the electrophilic and nucleophilic sites for the title Molecule, MEP was calculated using the B3LYP/LanL2DZ method with the 6-31++G(d,p) basis set and optimized geometries. The negative (red) regions of MEP were related to electrophilic reactivity and the positive (blue) regions to nucleophilic reactivity. The MEP maps of $\mathbf{L_1}$ and complex **1** were shown in **Figure 3 (a) - (d)**. The negative regions (deep red) are mainly over the electronegative atoms such as hydroxyl oxygen and azomethine nitrogen. The carbon and hydrogen atom bears the positive charge and is shown in blue/green colour. The electrostatic potential in ligand $\mathbf{L_1}$ ranges between -6.222×10^{-2} to 6.222×10^{-2} au, in $\mathbf{L_2}$ –0.107 to 0.107 au. In complex **1** it ranges from –0.111 to 0.111 au. Similarly, in Complex **2**, potential values were observed as –0.103 to 0.103au. The different values of the electrostatic potential at the surface are represented by different colours. The potential increases in the order: red < orange < yellow < green < blue [25].

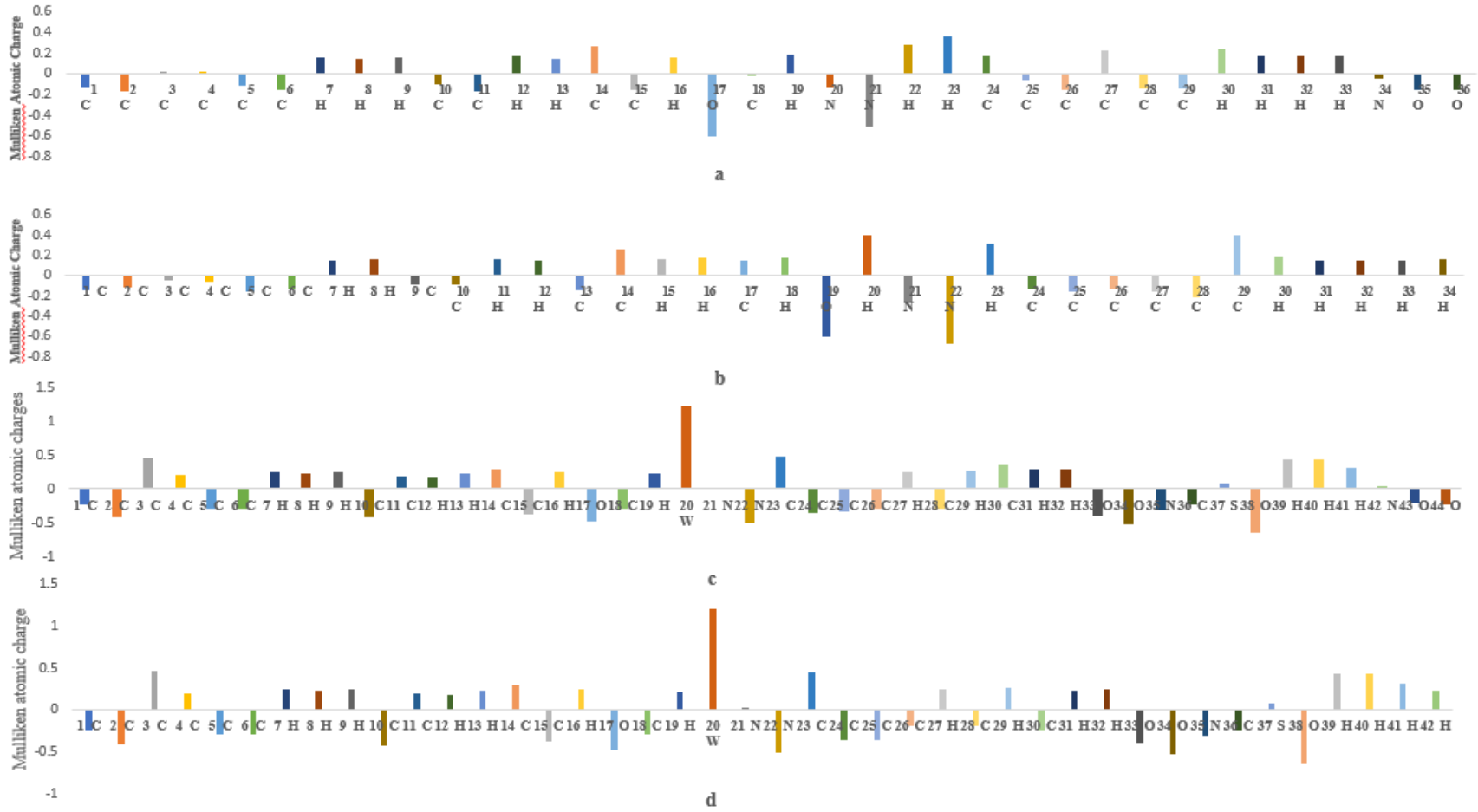

Figure 2: Mulliken atomic charge plot of (a) L_1 (b) L_2 (c) complex 1 (d) complex 2

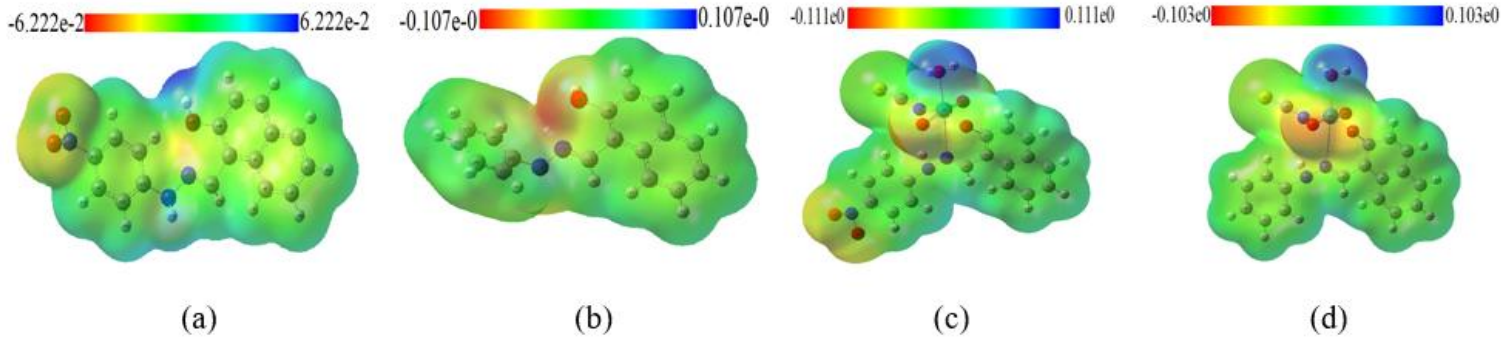

Figure 3. Molecular Electrostatic Potential (MEP) of (a) L_1 (b) L_2 (c) complex 1 (d) complex 2

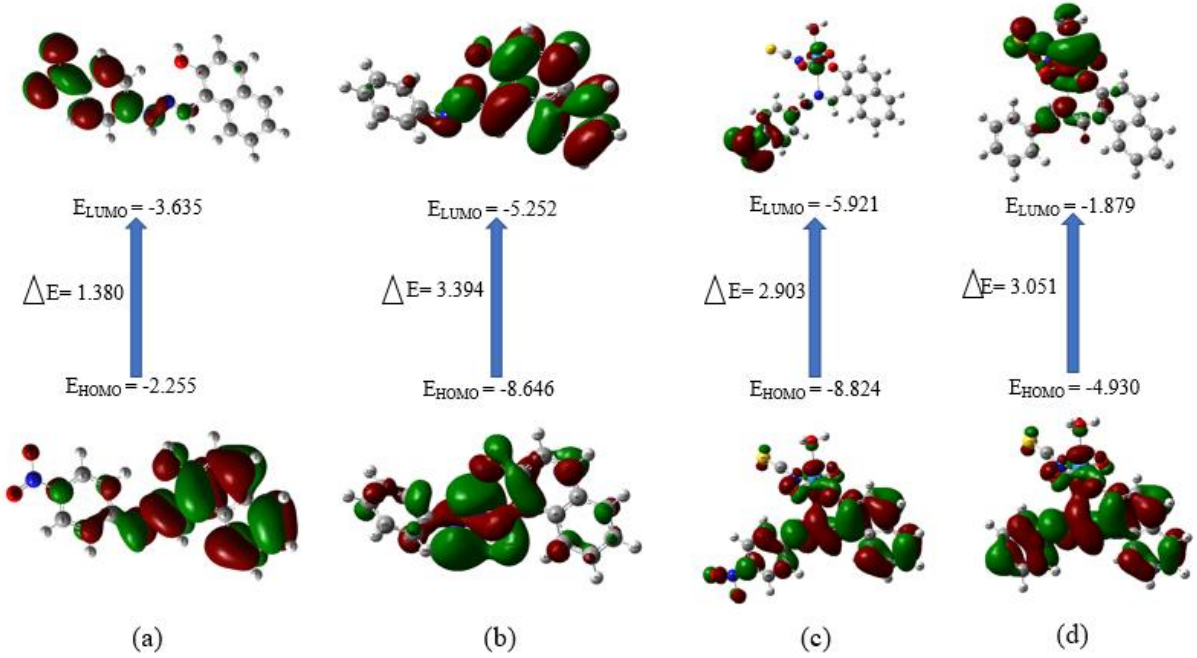

Figure 4. HOMO-LUMO structure with energy level diagram of (a) L_1 (b) L_2 (c) complex 1 (d) complex 2

Frontier Molecular orbitals analysis

HOMO and LUMO are two important molecular orbitals that are deduced for ligand **L_1** and complex **1**. The chemical stability of the complexes was established by the difference in energy (ΔE) between HOMO and LUMO. Complex with larger energy difference has a lower chemical reactivity. A suitable cavity was formed for encapsulating W(VI) by the Schiff base ligand and the heterocyclic ring was used as the anchoring co-ligand. The computed HOMO energy values of the **L_1** and complex **1** were -3.635 eV and -8.824 eV (**Figure 4**). The LUMO energy of the **L_1** and complex **1** were found to be -2.255 eV and -5.921 eV. Since complex **1** exhibit the highest ΔE, it is likely to have the highest stability. From the calculated energies of the highest occupied Molecular orbital (HOMO) and lowest unoccupied Molecular orbital (LUMO), it may be concluded that:

1. The difference of FMOs energies in complexes for E_{HOMO} is in the order **1 > L_2 > 2 > L_1**, and for E_{LUMO} the order is **1 > L_2 > L_1 > 2**.
2. Complex **1** has low values of the energy gap (ΔE) than complex **2**suggesting low stability and high reactivity.
3. Complex **1**exhibit a high value of the dipole moment than complex **2**, which may favour dipole-dipole interactions between molecules.

Bond parameters

In the absence of a single crystal, it was essential to optimize the molecular structure of ligands and complex **1-2** in the ground state. The optimized bond lengths and bond angles of investigated compounds were listed in **Tables 2** and **3** following the atom numbering scheme. The optimized geometrical parameters of the ligand were compared with complexes. The optimized C-O bond length was 1.4329 Å in **L_1** and 1.4316 in **L_2**, but in complexes, it was slightly increased indicating a weaker C-O bond. The optimized O-H bond length in **L_1** was 0.9680Å which was diminished in complexes. The bond length of azomethine -HC=N in ligand was found to be 1.293 Å, which shows an increase of 0.037-0.042 Å in the complexes. This increase in bond distance was because of the transfer of double-bond electron density towards metal and a decrease in the double bond character of C=N, which in turn confirms the coordination of metal with azomethine-N. Unequal bond lengths of W-N and W-O were also responsible for the slight deviation. From the bond angle data (**Table 22**) it was also observed that in complexes O=W=O, O-W=O, and N-C-S bond angles have slightly deviated. From the bond length and bond angle data, it was revealed that complexes were almost octahedral with slight distortion.

Table 2: Geometrically optimized bond lengths of ligands and complexes

Parameters	**L_1**	**L_2**	**Complex 1**	**Complex 2**
C-O	(C14-O17)1.432	(C14-O19)1.430	(C14-O17)1.60	(C14-O17)1.41
H-O	(O17-H18) 0.968	(O19-H20) 0.960	-	-
C=N (imine)	(C18=N20)1.293	(C17=N21)1.280	(C18=N20)1.332	(C18=N20)1.317
C-C	(C14-C11)1.404	(C14-C09)1.440	(C22-C23)1.40	(C11-C18)1.40
C-N	(C24-N21)1.470	(C29-N22)1.469	(C22-N21)1.55	(C22-N21)1.28
N-O	(N34-O35)1.320	-	(N42-O43)1.34	-
W-O	-	-	(W33-O35)2.013	(W34-O36)2.015
W=O	-	-	(W33-O17)1.612	(W34-O17)1.613
W-N	-	-	(W33-N20)2.79	(W34-N20) 3.33

Table 3. Geometrically optimized bond angle of ligands and complexes

Angle	L_1	L_2	Complex **1**	Complex **2**
∠C-C-O	(∠C15-C14-O17) 120.086	(∠C13-C14-O19) 120.061	(∠C15-C14-O17) 122.99	(∠C15-C14-O17) 122.99
∠C-O-H	(∠C14-O17-H23) 109.471	(∠C14-O19-H20) 109.567	-	-
∠C=N-N (hydrazine)	(∠C18-N20-N21) 120.281	(∠C17-N21-N22) 120.371	(∠C18-N20-N21) 141.96	(∠C22-N21-N20) 149.18
∠H-C=N (imine)	(∠H19-C18-N20) 109.419	(∠H18-C17-N21) 120.509	(∠H19-C18-N20) 123.52	(∠H19-C18-N20) 123.91
∠C-N-H	(∠C29-N22-H23) 120.786	(∠C29-N22-H23) 119.676	(∠C22-N21-H32) 126.92	(∠C22-N21-H33) 122.79
∠C-C-H	(∠C6-C5-H12)120.819	(∠C1-C2-H3)119.991	(∠C1-C2-H9)120.05	(∠C1-C2-H9)120.05
∠C-N-O	(∠C27-N34-O36) 132.205	-	(∠C29-N42-O43) 119.32	-
∠N(imine)-W-N	-	-	(∠N28-W33-N36) 161.89	(∠N20-W34-N37) 153.68
∠O=W =O	-	-	(∠O34-W33-O35) 168.68	(∠O35-W34-O36) 150.96
∠O- W =O	-	-	(∠O17-W33-O37) 170.228	(∠O17-W34-O35) 169.34
∠N=C=S	-	-	∠N37-C38-S40) 153.49	∠N38-C39-S41) 154.96

Characterization of W(VI) complexes

The stoichiometries of ligands and complexes were in agreement with elemental analyses. ESI-MS of ligands and complexes shows several peaks depending upon the fragmentation pattern. The pseudo molecular ion peak observed at *m/z*= 307.268 attributed for $[C_{17}H_{13}N_3O_3 + H^+]^+$ indicates the molecular mass of $\mathbf{L_1}$. The ESI-MS of $\mathbf{L_1}$ is given in **Figure 5**. ESI-Mass spectra of complexes exhibit several peaks. However, a pseudo molecular ion peak for $[M+H^+]$ was inevitably present in each case, which indicates the molecular mass.ESI-MS of complex **1-2**is given in **Figures 5** and **6**. The lower value of molar conductance (Λ_m) of metal complexes is indicative of their non-electrolytic nature [26].

FT-IR spectra

FTIR spectra of ligands displayed peaks at ~ 3490 cm^{-1}, 3365 cm^{-1}, 1622 cm^{-1}, 1273 cm^{-1} attributed for ν(OH), ν(NH), ν(CH=N) and ν(C-O). In $\mathbf{L_1}$a peak at 1284 cm^{-1} was additionally present, assigned for ν(NO_2). In complexes, the broad peak at 3490 cm^{-1} has vanished and a new peak at 560 cm^{-1} appeared due to the emergence of ν(W-O) bond [27]. The presence of signals at 2066 cm^{-1}, 784 $cm^{-1,}$ and 470 cm^{-1} was attributed to the presence of ν(C=N), ν(C=S), and δ(NCS) vibrations confirming the presence of isothiocyanate moiety. Tungsten, being a hard metal, coordinates with the thiocyanate group through the nitrogen atom[28]. The signal at 1622 cm^{-1} in ligand attributed for ν(CH=N) vibration was slightly shifted in ligands (~ 5 cm^{-1}) to lower wave number confirming the coordination of the azomethine group to metal[29]. A new peak expected at ~450 cm^{-1} for ν(W-O) was mixed with δ(NCS) vibration of the NCS group. The IR spectra of both complexes exhibit bands at ~ 870 cm^{-1} and ~ 960 cm^{-1} due to vibrations of (O=W=O)sym and (O=W=O)assym modes respectively, indicating the presence of cis-WO_2 structure[30, 31].

Significant IR vibrations are given in Table 3.

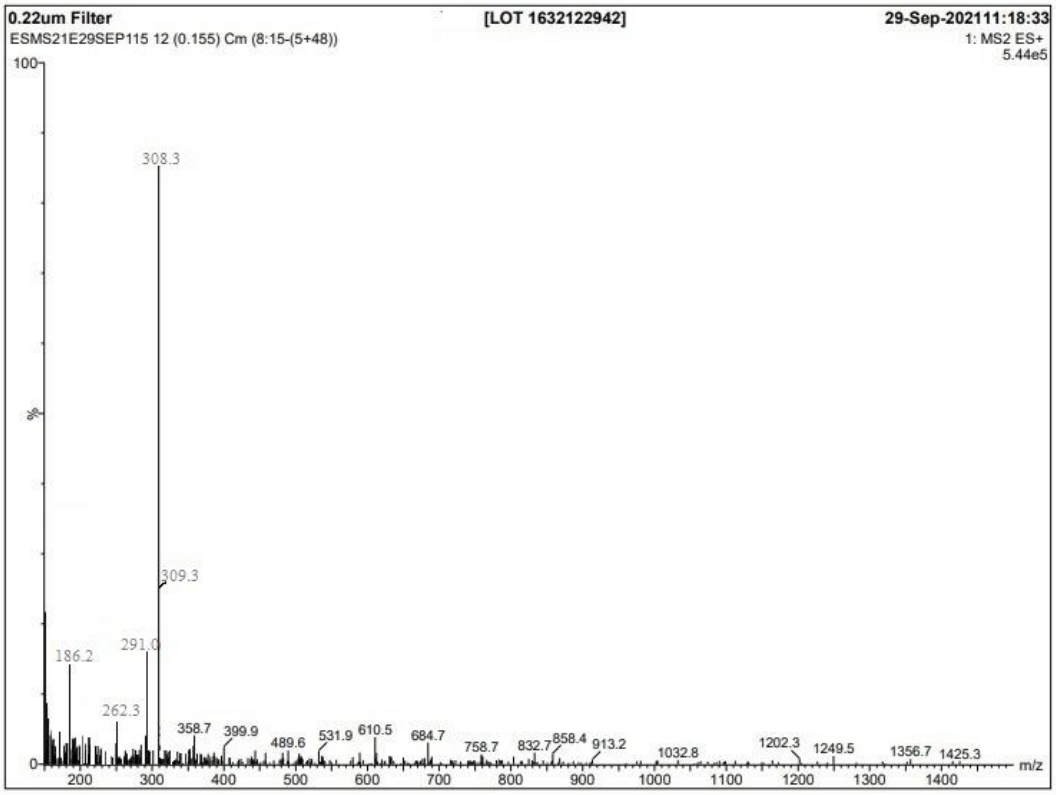

Figure 5. ESI-MS of ligand L_1

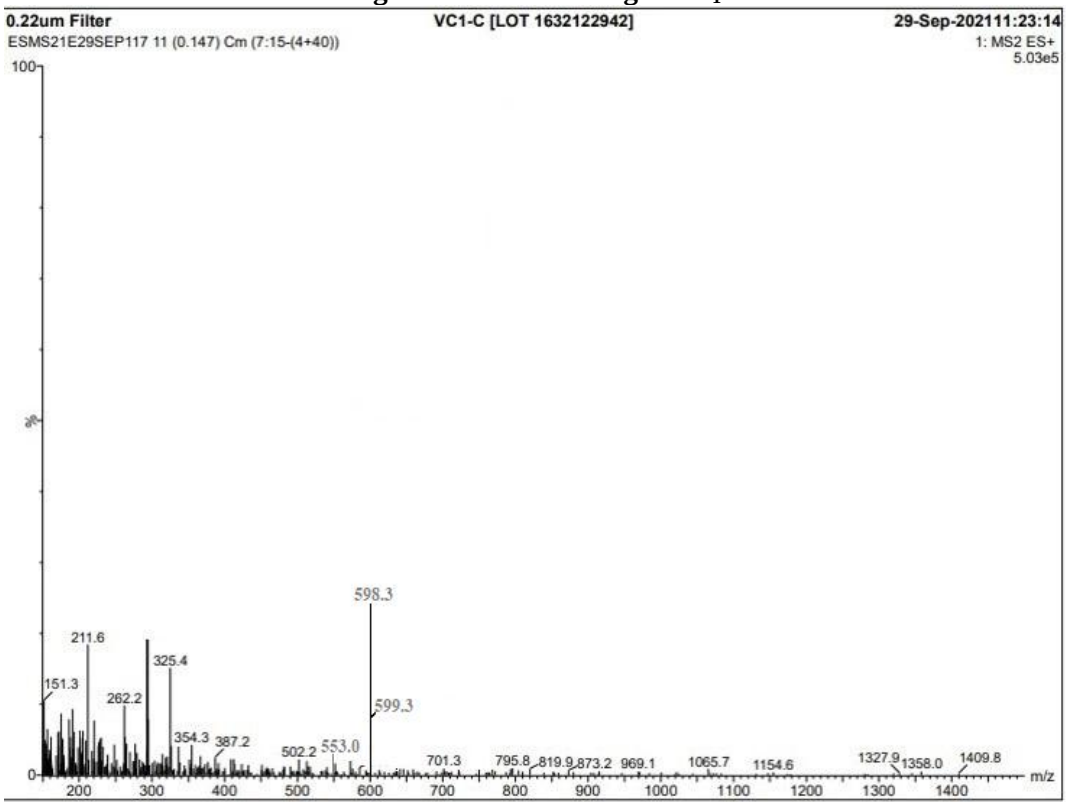

Figure 6. ESI-MS of ligand complex 1

Table 4. Significant IR vibrations (in cm^{-1}) in ligands and complexes

S.No.	Ligand	ν(OH)	ν(NH)	ν(C=N)	ν(CH=N)	ν(NO_2)	ν(C-O)	ν($O=W=O)_{as}$	ν($O=W=O)_s$	ν(C=S)	ν(W-O)	δ(NCS)s+ ν(W-N)
1	L_1	3492	3365	-	1622	1284	1273	-	-	-	-	
2	L_2	3490	3361	-	1620	-	1281	-	-	-	-	
3	Complex 1	-	3356	2069	1617	1281	1270	958	869	784	560	473
4	Complex 2	-	3357	2066	1616	-	1274	954	866	783	557	470

The FT-IR spectra of **L_1** and complex **1** were correlated with the experimental (solid phase) and theoretical data (gas phase) (**Table 5**). FT-IR experimental and theoretical spectrum of **L_1** is given in **Figure 7**. The calculated frequencies were slightly shifted from the experimental values of the normal vibrations. DFT calculation generally overestimates the frequencies and neglects the crystal packing effects. However, anharmonicity, as well as incompleteness of the basis set and dynamic electronic correlation, were also responsible for the above-stated deviations. Therefore, we have derived scaling factors and applied them to get a satisfactory value. The gas-phase FT-IR frequencies in compounds were recorded with B3LYP and 6-311G basic set, the scaling factor for **L_1** was determined as 1.017 (R^2 = 0.9959) over a complete range of the spectrum, and in complex **1** it is 0.9906 (R^2 = 0.9977). The theoretical and experimental FT-IR spectrum of complex **1** is shown in **Figure 8**.

The experimental FT-IR spectrum of **L_1** exhibits a band at 3492 cm^{-1}, attributed to hydroxyl OH stretching vibration. In the theoretical FT-IR spectrum, it was observed at an unscaled frequency of 3497 cm^{-1}. The scaled vibrational frequency due to OH stretching was derived and found to be 3493 cm^{-1} with a percentage deviation of 0.1 %. In complex **1** this band was absent and a new band at a lower frequency appeared at 560 cm^{-1} assigned for ν(W-O). However, in the theoretical FT-IR spectrum, this stretching band was observed at the scaled frequency region of 871 cm^{-1} with a deviation of 0.2 %. In the experimental FT-IR, of complex **1**, the appearance of a new band due to W-N stretching observed at 473 cm^{-1} confirms the coordination of metal ions with azomethine-N. The correlation of the experimental FT-IR spectrum with the theoretical IR spectrum for **L_1** and complex **1** is given in **Figure 9**. In heterocyclic compounds, the N-H stretching vibrations occur in the region 3500-3000 cm^{-1} [32]. The FT-IR band appeared at 3365 cm^{-1} of the title compound and has been assigned to N-H stretching modes of vibrations. In complex **1**, the experimental value for the N-H vibration stretching band was observed at 3356 cm^{-1}. However, in theoretical spectra, this band was quite close to the experimental value and observed at a scaled frequency region of 3347 cm^{-1} with a deviation of 0.1%. The HC=N peak of **L_1** appeared in the region of 1622 cm^{-1}. The presence of this band also confirms the formation of azomethine moiety in the ligand. In theoretical FT-IR spectra, it was observed at an unscaled frequency of 1616 cm^{-1}. However, after scaling this band was found to be at 1624 cm^{-1} with a percentage deviation of 0.3 %. In complex **1** this band was shifted downwards and observed at 1617cm^{-1}, which confirms the coordination of azomethine nitrogen with metal [33]. In the theoretical FT-IR, the band due to HC=N moiety in complex **1** was observed at a scaled frequency of 1618 cm^{-1} with a percentage deviation of 0.1 %.

Table 4. Correlation of experimental FT-IR spectra with theoretical IR spectra for $\mathbf{L_1}$and Complex **1**

L_1					***Complex 1***			
Peak assignment	**Experimental**	**Theoretical**		**% deviation**	**Experimental**	**Theoretical**		**%deviation**
		Unscaled	**scaled**			**Unscaled**	**Scaled**	
ν(OH)	3492	3497	3493	0.1	-	-	-	-
ν(NH)	3365	3351	3367	0.1	3356	3341	3147	0.1
ν(C=N)	1622	1616	1624	0.3	1617	1609	1618	0.5
ν(NO_2)	1284	1279	1287	0.6	1281	1275	1284	0.7
ν(C-O)	1273	1268	1274	0.6	1270	1267	1276	0.7
ν(O=W=O) as	-	-	-	-	958	952	961	0.9
ν(O=W=O)s	-	-	-	-	869	863	871	0.9
ν(C=S)	-	-	-	-	784	782	787	0.6
ν(M-O)	-				560	578	570	

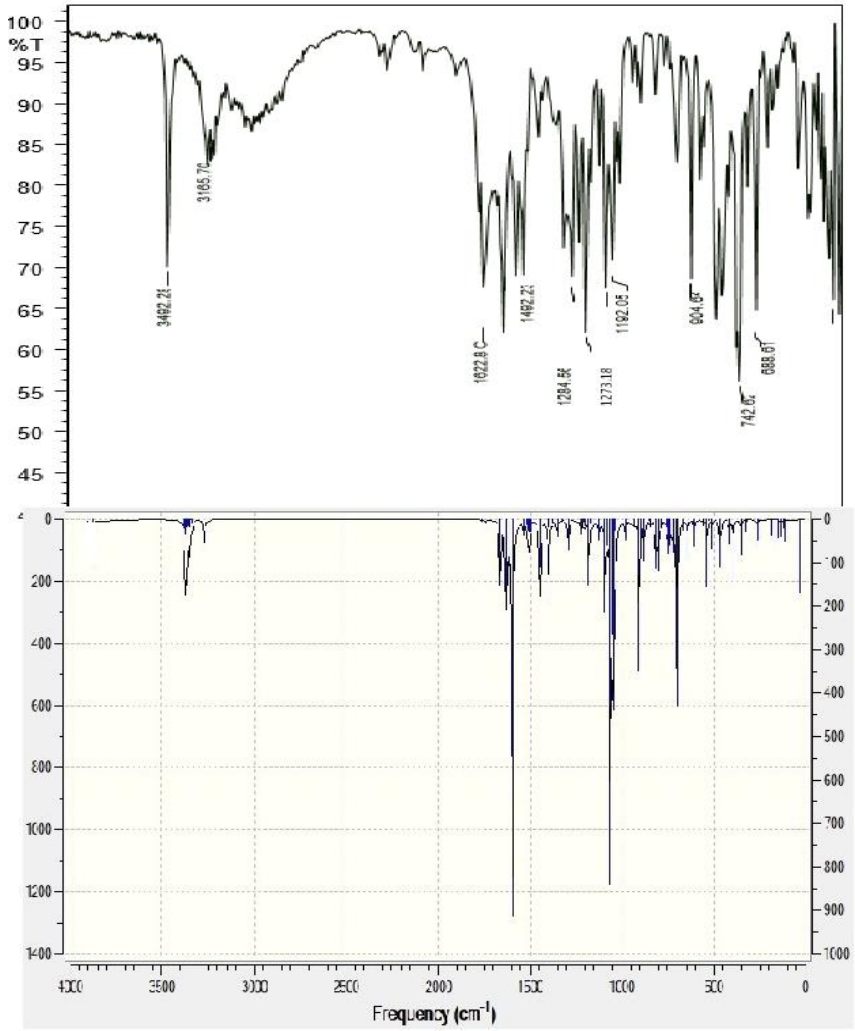

Figure 7: FT-IR experimental (above) and theoretical (below) spectrum of $\mathbf{L_1}$

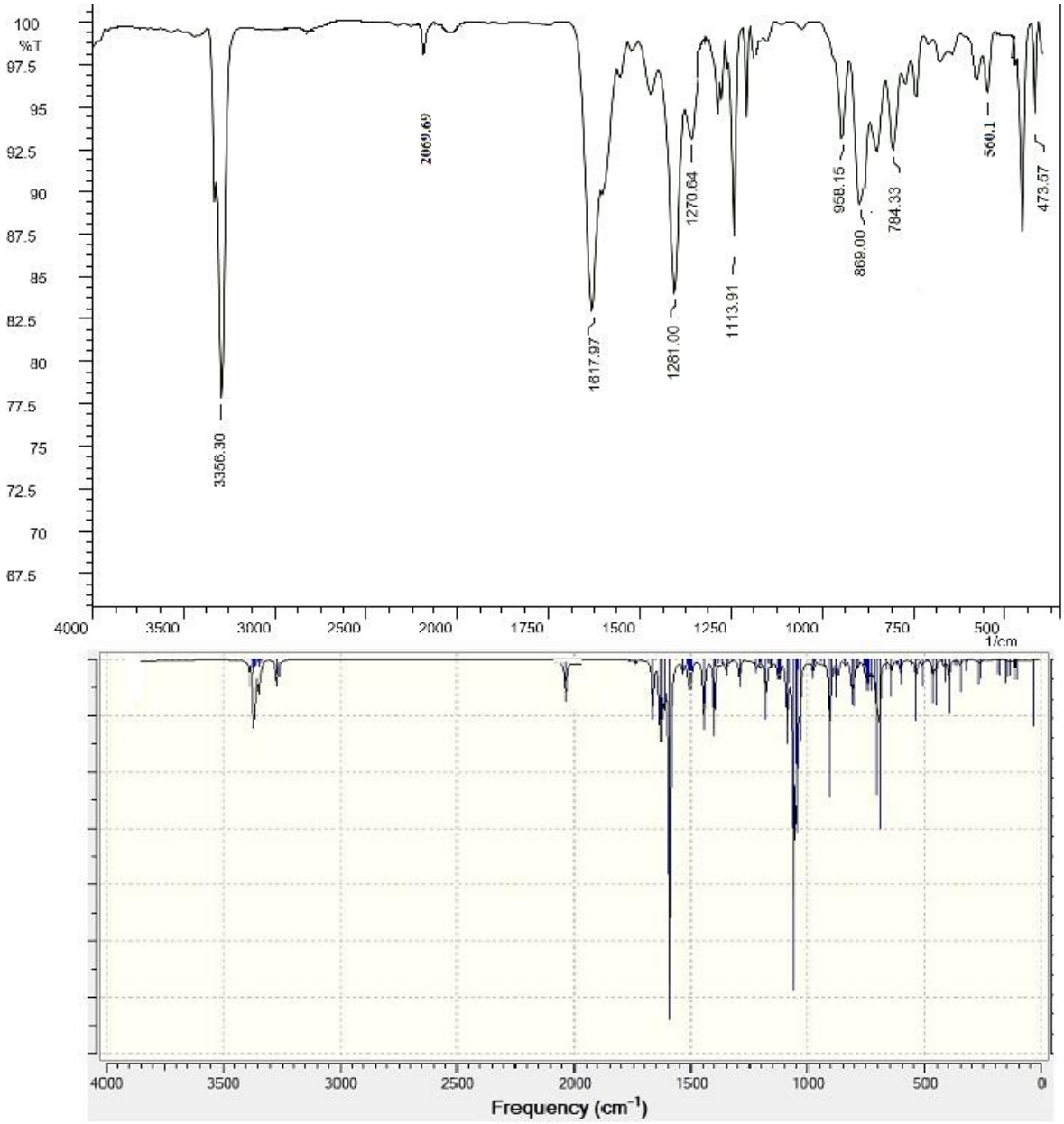

Figure 8. FT-IR experimental (above) and theoretical (below) spectrum of complex 1

Electronic spectra

In the UV–Vis spectra of ligands four absorption bands were observed. The first two bands observed between 210 – 240 nm were assigned to the intra-ligand π→ π* transition and another two strong absorption bands between 270 - 290 nm were ascribed to intra ligand n→ π* transition associated with imine moiety. The shift of this n→ π* transition to a higher wavelength (~20 nm) in the spectra of the metal complexes suggests the coordination of azomethine nitrogen to the metal. However, in the complexes one/two appeared between 330 – 375 nm were assigned for the ligand to metal charge transfer (LMCT) transitions [34]. UV-Vis spectra of the $\mathbf{L_1}$, $\mathbf{L_2}$, and Complex **1-2** are given in **Figure 10(a-d)**. The magnetic susceptibility measurements of the complexes showed that all the complexes are diamagnetic as expected for W(VI) complexes. Electronic spectral data was suggestive of octahedral geometry around W(VI) ion[35].

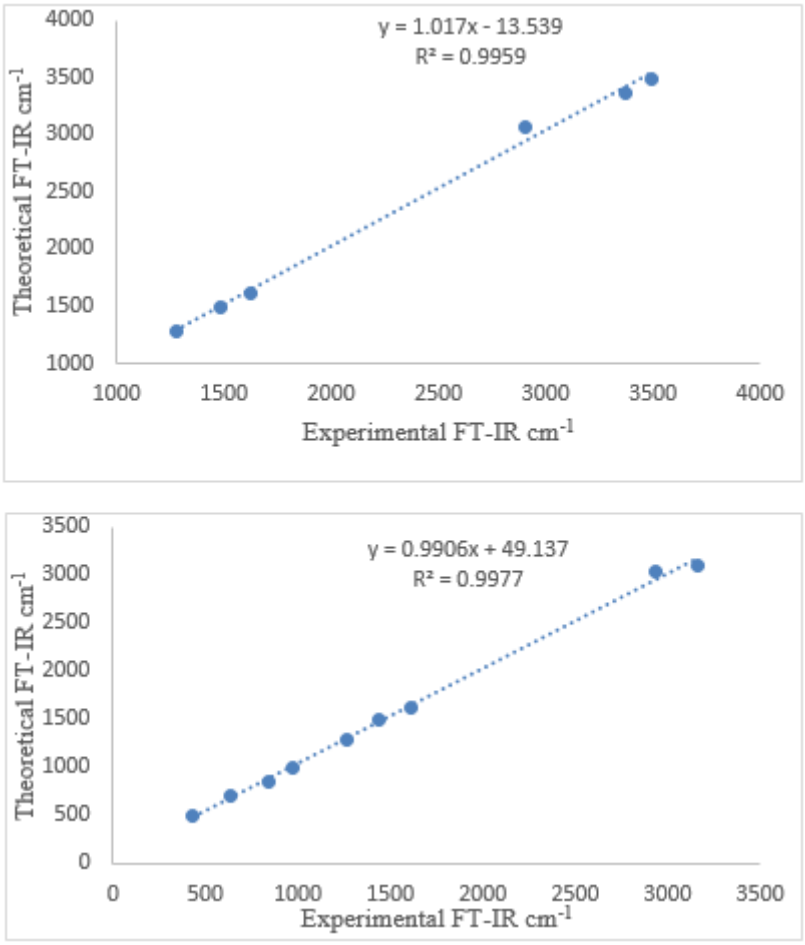

Figure 9. Correlation of experimental FT-IR spectrum with theoretical IR spectrum for (a) L_1 and (b) complex 1

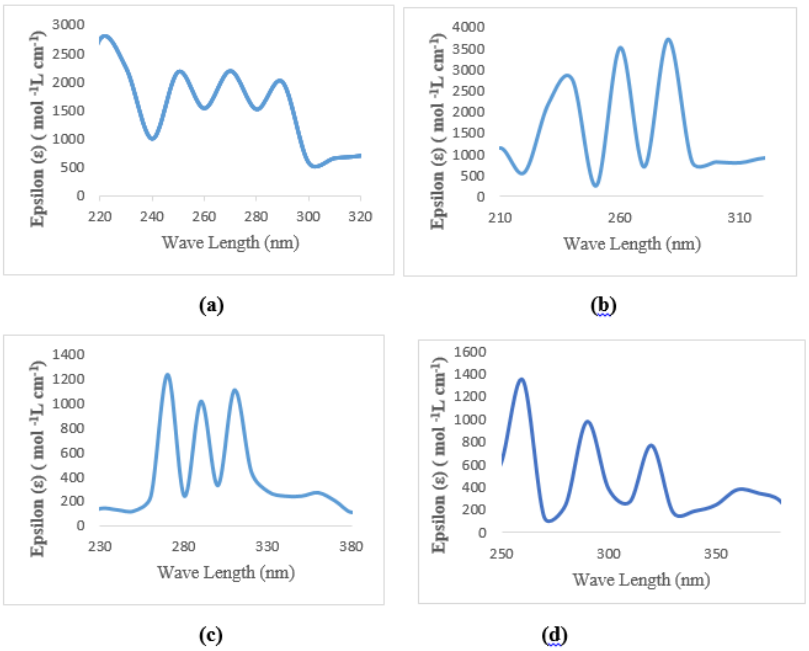

Figure 10. UV-Vis spectra of the L_1, L_2, and Complex 1-2 are given in (a-d).

[1]H-NMR spectra

In [1]H-NMR of ligand, the deshielded signal appeared at δ 10.812 ppm and was attributed to phenyl hydrazine –NH. The signal observed at δ 8.891 for 1H was assigned for azomethine (-CH=N-) proton. The presence of this signal was positive evidence for the formation of the Schiff base ligand [36]. The two triplets centered at ~ δ 7.962 and δ 7.392 ppm for one proton each and two doublets centered at ~ δ 8.323 and δ 7.811 ppm for one proton each were assigned for phenyl ring protons. The three aromatic protons of the naphthalene ring appeared as two doublets centered at δ7.810, 7.897 ppm. The [1]H-NMR spectrum of the ligand is given in **Figure 11**. The theoretical chemical shift values were calculated by the GIAO method using TMS HF/6-31G(d) GIAO and TMS B3LYP/6-311+G(2d,p) GIAO level theory. For [1]H-NMR of ligand calculated correlation coefficient is $\delta_{cal} = 1.0948\delta_{exp} + 0.0384$ ($R^2 = 0.9626$).

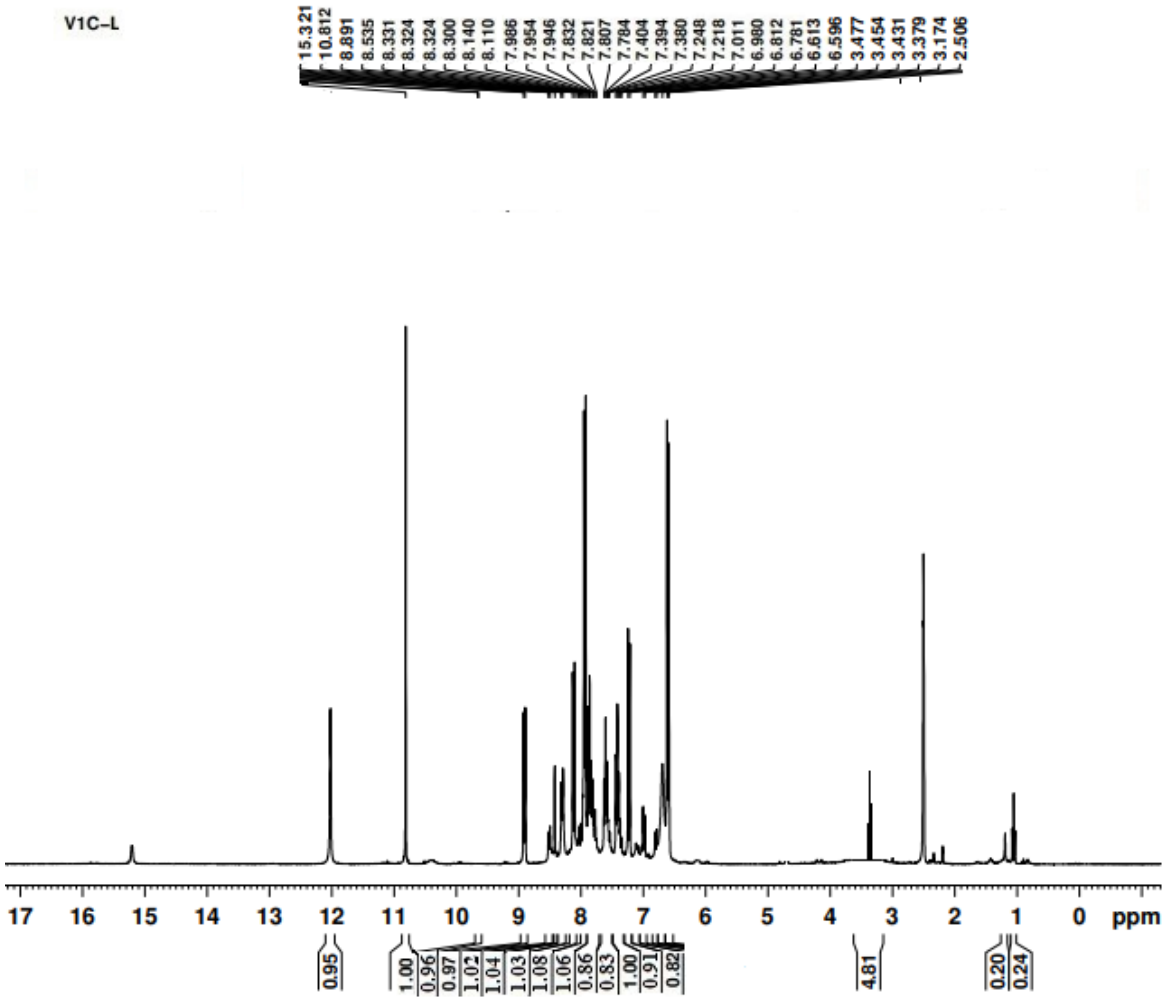

Figure 11. [1]H-NMR of L_1

The coordination of the azomethine HC=N group was confirmed by the downfield shifting of signal in complexes by δ 0.037 - 0.086 ppm attributed to the discharging of the electronic cloud towards the W(VI) ion [37]. The hydroxyl OH proton signal observed at δ 15.321 in the ligand disappeared in the spectra of complexes, indicating deprotonation and coordination of the oxygen with the metal ion[38]. One signal that appeared at ~ δ 10.820 ppm in complexes **1** and **2** was attributed to the NH proton of phenyl hydrazinering[39]. In complexes two multiplets centered at ~ δ 7.500 and δ7.300 ppm for three protons each, were attributed to the phenolic moiety of ligand. However, four protons of hydrazine moiety were

manifested as four doublets centered at ~δ 8.450, ~δ 7.80, ~δ 7.760, and ~δ 6.950 ppm. The ^{1}H-NMR spectrum of complex **1** is given in **Figure 12**. The theoretical chemical shift values were calculated by the GIAO method using TMS HF/6-31G(d) GIAO and TMS B3LYP/6-311+G(2d,p) GIAO level theory. The ^{1}H-NMR correlation coefficient R^2 for complex**1** was determined as 0.9577 (δ_{cal} = 1.0488δ_{exp} - 0.098).

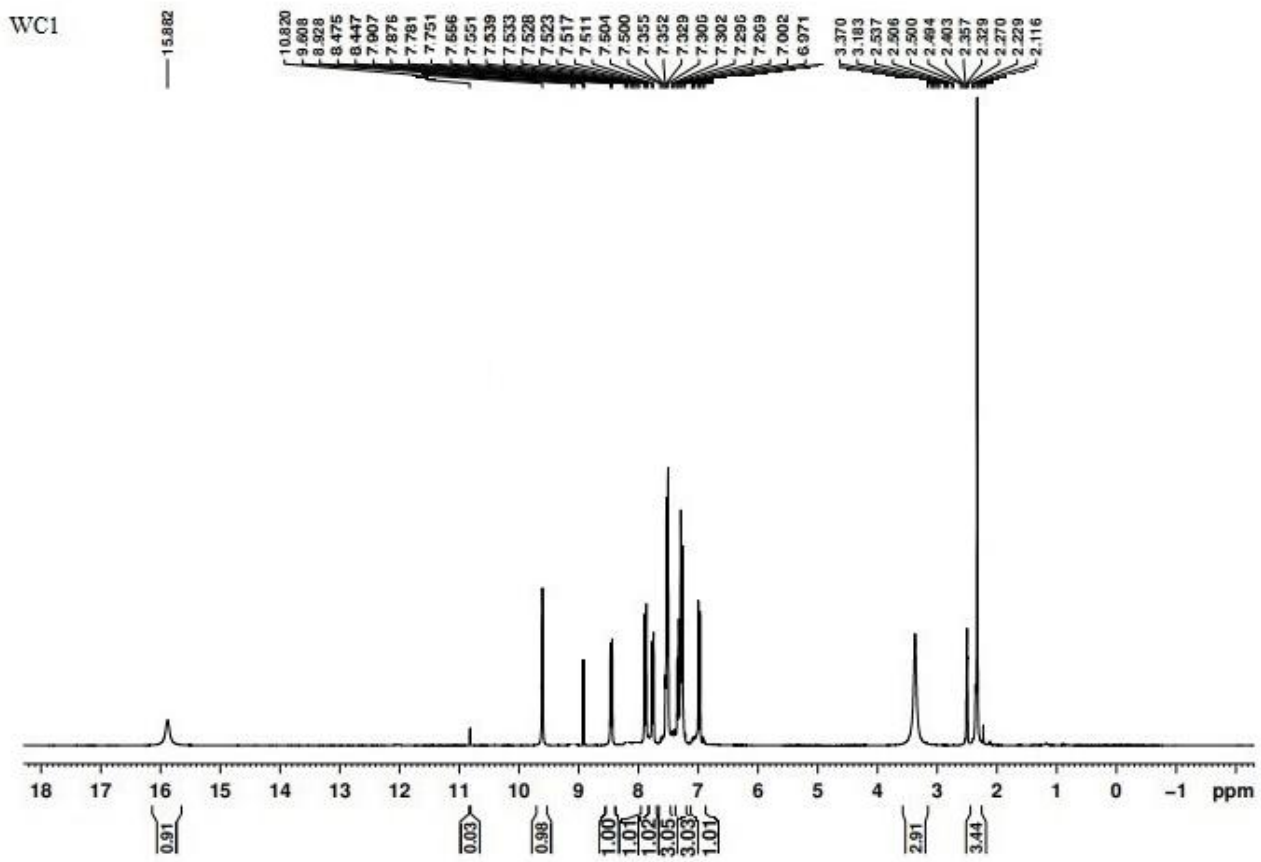

Figure 12. ^{1}H-NMR of complex 1

$^{13}C\{^{1}H\}$-NMR spectra

In ^{13}C-NMR formation of azomethine linkage in the ligand is confirmed by the presence of a signal at ~ δ 171.0 ppm attributed to azomethine carbon. A signal at δ 162.0 ppm in ligands was assigned for the carbon linked with the hydroxyl group. Ten signals observed between δ 162.0 - 128.0 ppm were ascribed for aromatic carbon of phenolic moiety. Similarly, six signals between δ 126.0-121.0 ppm were assigned for the substituted phenyl group. The ^{13}C-NMR spectrum of $\mathbf{L_1}$ is given in **Figure 12**. The correlation coefficient R^2 of $\mathbf{L_1}$ for ^{13}C-NMR was determined as 0.9626. The signals observed at ~ δ 171.1 ppm in ligands for >HC=N carbon was downfield shifted by 4.26 - 5.61 ppm in the complexes confirming the transfer of one lone pair electron from nitrogen to the metal and coordination of >C=N to metal. The signal at δ 163.0 ppm for the C-O group in ligand was downfield shifted and appeared ~ δ 156.0 ppm in the complexes. The ten signals for aromatic carbon of phenolic moiety were observed between δ 156.0-127.0 ppm. The five signals observed between δ126.0 - δ122.0 ppm were ascribed to substituted aromatic carbon. The ^{13}C-NMRspectra of complex **1** are given in **Figure 13**. The correlation coefficients of ^{13}C-NMR for complex **1** were determined as 0.997.

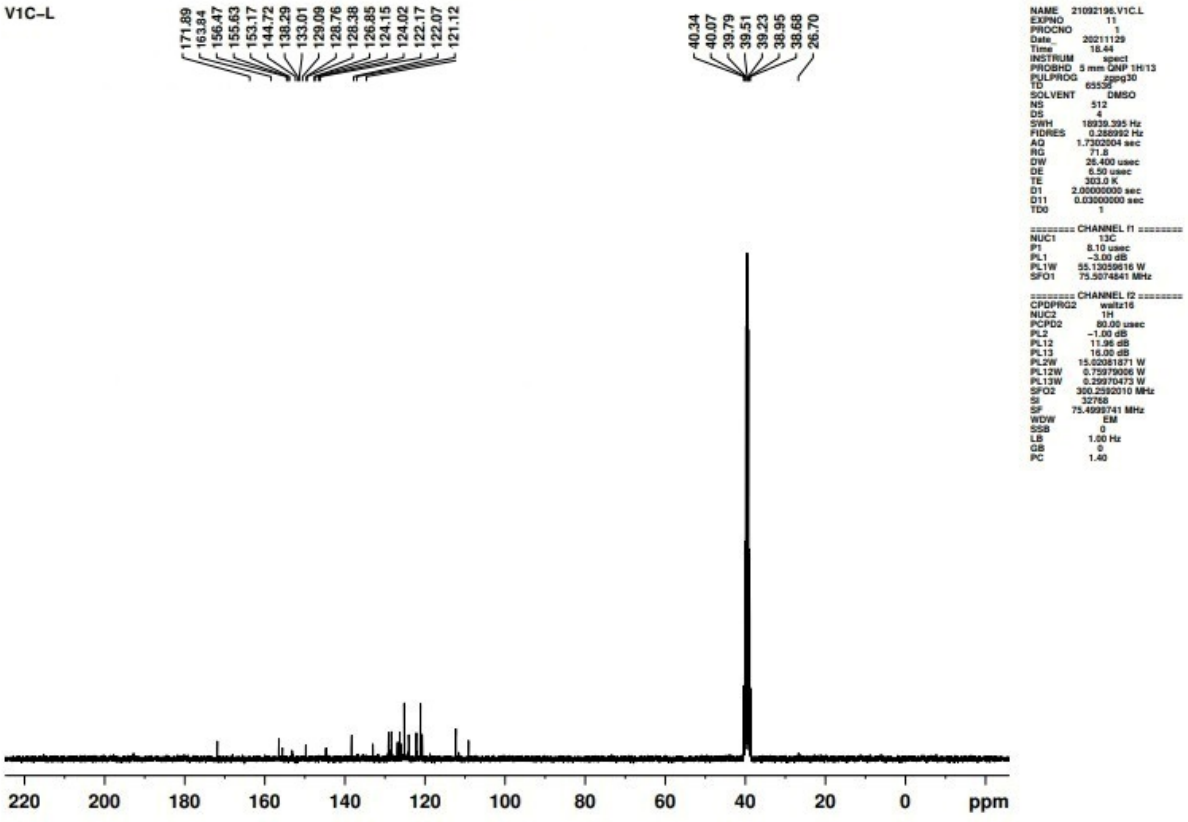

Figure 12. ^{13}C-NMR of L_1

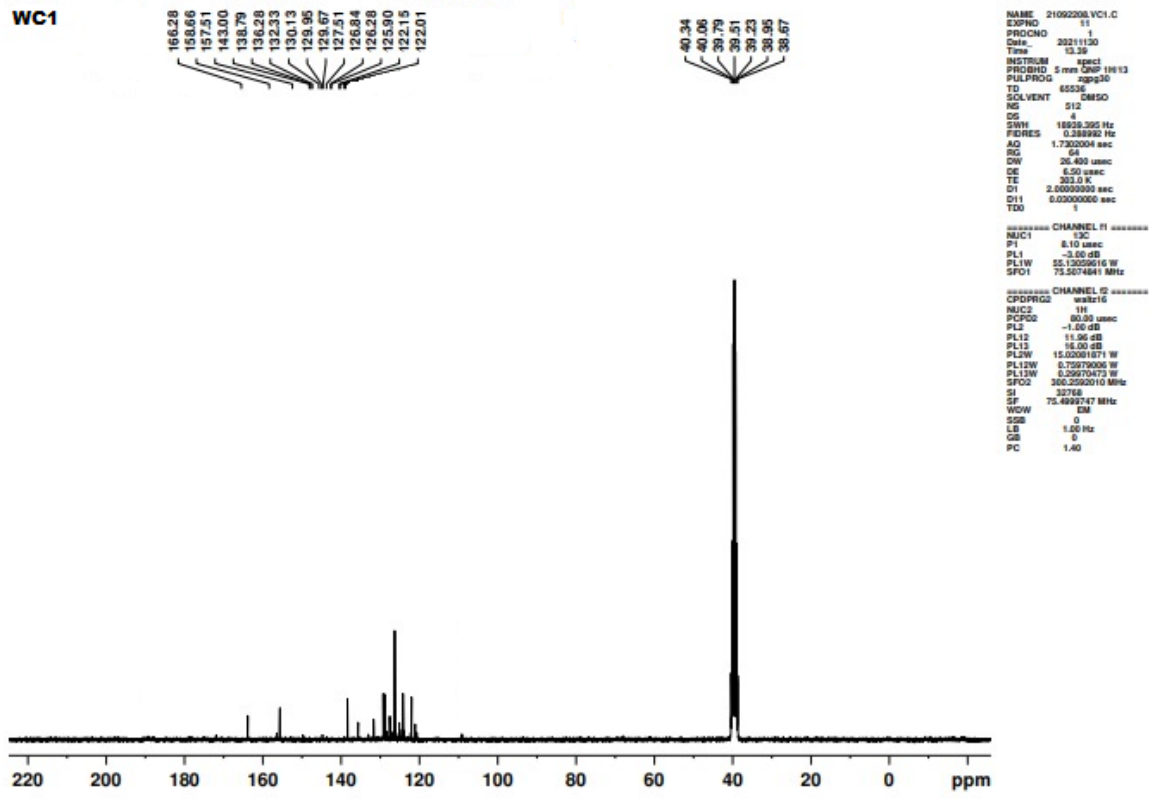

Figure 13. ^{13}C-NMR of Complex 1

Thus based on elemental analysis, ESI-MS, FTIR, ^{1}H-NMR, ^{13}C-NMR, and DFT the most plausible Chemdraw and DFT optimized structures are given below.

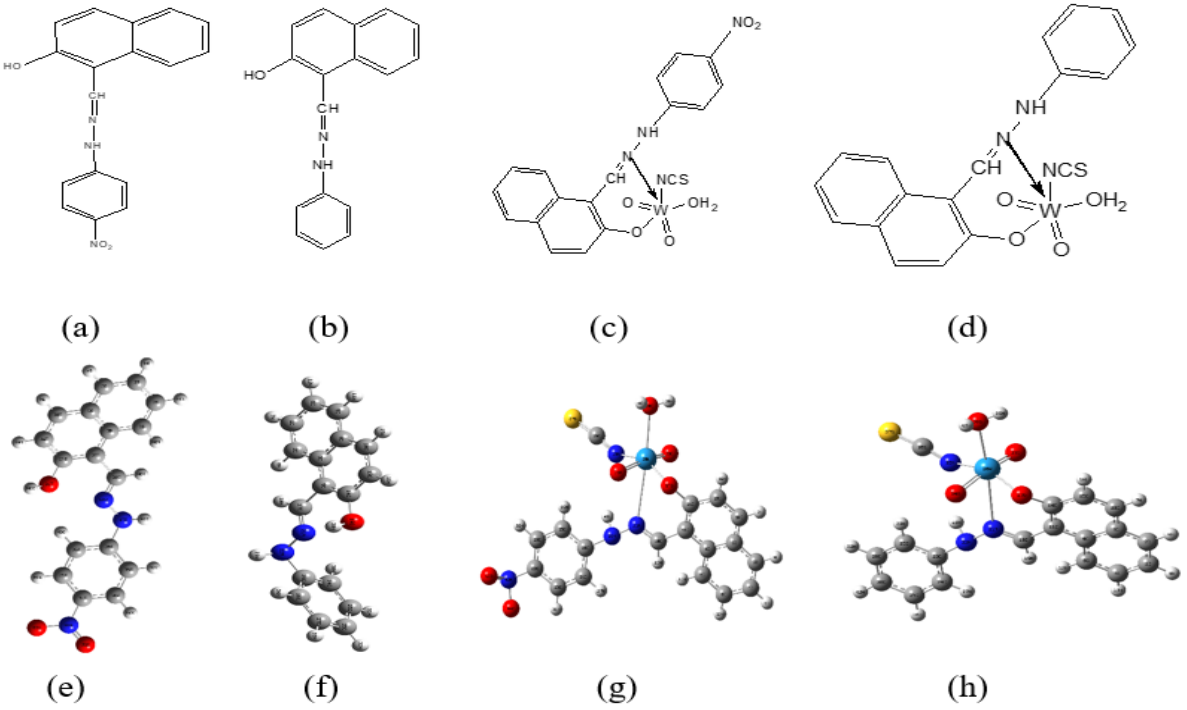

Figure 14. Chemdraw structure of (a) L_1 (b) L_2 (c) Complex 1 (d) Complex 2 and DFT optimized structure of (e) L_1 (f) L_2 (g) Complex 1 (h) Complex 2

Antimicrobial assessments

The results of the *in vitro* antimicrobial activity of the **L_1, L_2,** and complex **1-2** are presented in **Table 2**. All complexes displayed were activity than Schiff base against *Escherichia coli*. The higher activity of complexes could be explained based on the increase in lipophilic character in complexes and also due to the presence of the W(VI) nucleus which could provide the ability of such complexes to pass through the lipid layer of lipoprotein bacterial cell membrane[40]. In *Escherichia coli*, complex **2** has displayed antibacterial activity almost near to the standard drug.

Table 2. Antimicrobial activity of L_1, L_2 and complex 1-2

S. No	Complex/Ligand	Activity against *E. Coli*	*Inhibition Zone in mm
1	L_1	+	17
2	L_2	+	24
3	Complex **1**	+	36
4	Complex **2**	+	39
5	Chloramphenicol	+	40

Anticorrosion activity

Corrosion inhibition study of ligand**s** and their complexes **1-2** were performed by using weight loss measurement. The concentration of both was chosen to be 50 ppm. From **Figure** 15 it was observed that complex **2** exhibits the lowest corrosion rate and highest corrosion inhibition efficiency than other complexes probably due to the presence of imidazole moiety. The presence of electron donors N and O in complexes increases electron density and thus better adsorption of complex **2** on the corroding surface,

which in turn increases the efficiency of corrosion inhibition. The corrosion inhibition efficiency rate follows the order **2** > L_1 > L_2 > **1**.

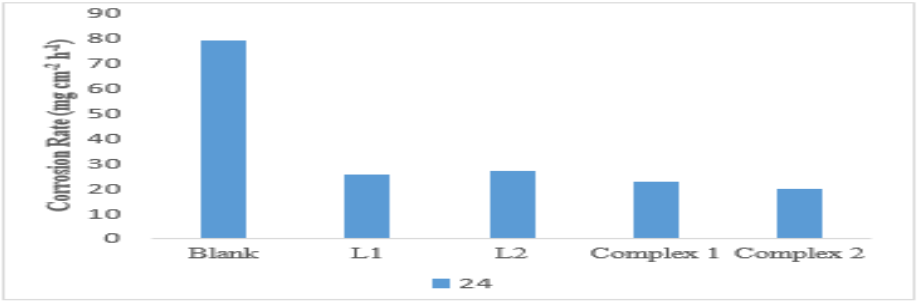

Figure 15. Corrosion rate of compounds

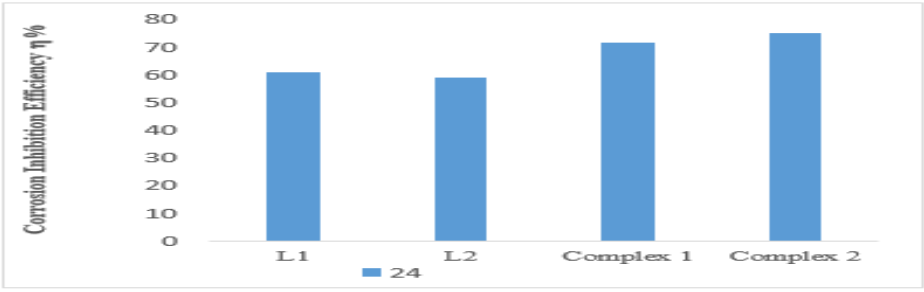

Figure 16: Corrosion inhibition efficiency of ligands and complexes

CONCLUSION

Two Schiff base ligands were synthesized and employed strategically in the synthesis of two novel dioxotungsten(VI) isothiocyanato complexes. Ligand and complexes were characterized experimentally by spectroscopic techniques and theoretically by DFT. The results from the DFT show that the calculated E_{HOMO}, $E_{LUMO,}$ and ΔE establish that the complexes possess good chemical reactivity and stability. In FT-IR and NMR spectra quite a good correlation has been observed in experimental and theoretical data. Octahedral geometry was suggested from spectroscopy. However, bond parameters from DFT suggest a slight distortion in bond length and bond angle. Antibacterial screening against *Escherichia coli* shows remarkable activity in comparison to the standard drugs at significantly lower MIC. Synthesized complexes were screened for anticorrosion activity and complex **2** manifested the highest anticorrosive activity.

ACKNOWLEDGEMENT

The authors are grateful to the **Principal,** Government Science College, Jabalpur, and the **HOD**, Chemistry Department, for providing laboratory facilities. We sincerely thank **SAIF-CDRI**, Lucknow, for recording ESI-MS spectra, ^{1}H-NMR, and ^{13}C-NMR. Author "**Vijay Chakravarti**" is grateful to Mr. Naveen Barsainya for his kind support.

REFERENCES

1. **Bevers LE, Hagedoorn PL, Hagen WR (2009).** The bioinorganic chemistry of tungsten. *Coordination Chemistry* **253** 269–290.
2. **Enemark JH, Young CG (1993)** Bioinorganic chemistry of pterin-containing Molybdenum and tungsten enzymes. *AdvInorgChem,* **40** 1-88.
3. **Lehninger AL (1979)** Biochemistry. *Kalyani Publishers,* New Delhi, **2** 481- 488.
4. **Coralia B, Crina K, Cătălin M, Constantin D, Gina VS, Luminiţa M, Larisa C, Mihaela B, Mariana C, Rodica O (2018).** Synthesis, Structural Characterization, Antimicrobial Activity, and In Vitro Biocompatibility of New Unsaturated Carboxylate Complexes with 2,2′-Bipyridine. *Molecules,* **23** 157.

5. **Reddy KH, (2011)** Coordination Compounds in Biology, *Resonance*, 4 67–77,
6. **Ali AM, Crouse KA, Saravanan N, Tarafder MTH (2001).** Coordination chemistry and biological activity of nickel(II) and copper(II) ion complexes with nitrogen–sulphur donor ligands derived from S-benzyldithiocarbazate, *Transition Metal Chemistry*, **26** 613–618.
7. **Kumar R, Mehani R, Singh DP, Verma SK (2006).** Synthesis and characterization of divalent metal complexes with ligand derived from the reaction of 4-aminopyridine and biacetyl, *Journal of Serbian Chemical Society*, 71 939.
8. **Deepa NT, Krishnan R, Madhu PK (2005).** Cadmium(II) complexes of 1,2-di(imino-4′-antipyrinyl)ethane, *Synth. React. Inorg Met. – Org. chem*, 35 883-888.
9. **Ali SA, Aboaly MM, Ramadan RM, Soliman AA (2002).** Chromium, Molybdenum and ruthenium complexes of 2-hydroxyacetophenone Schiff bases, *Journal of Coordination Chemistry*, 55 1161-1170
10. **Chowdhary V, Mehta RK, Parihar M, Ranga SP, Sharma S (1998).** Spectral and antibacterial investigation on tridentate Schiff bases and their Co(II), Cu(II) and Ni(II) complexes, *J Curr Bio Sci*, 5 98-100.
11. **Chohan H, Zahid H, (1999).** Biologically active transition metal complexes of Ni(II), Cu(II) and Zn(II) with2-aminothiazoleSchiff bases, *Met-Based Drugs*, 6 187-192.
12. **Chohan H, Zahid H (1999),** Ni(II), Cu(II) and Zn(II) metal chelates with thiazole Schiff bases synthesis, characterization, and bactericidal properties, *Met-Based Drugs*, 6 75-80.
13. **Kausar S, Zahid CH, (2001).** Synthesis, characterization and biological effect of anions on Co(II) and Ni(II) chelates of tridentate Schiff base, *J. Chem. Soc. Pak*, 23163-167.
14. **Jeffery GH, Bassett J, Mendham J, Denney RC (1989).** Vogel's textbook of quantitative inorganic analysis, 5th Edn, *John Wiley & Sons,* Inc. New York 463-464.
15. **Bridson BJ, Edwardm DA (1974).** *Inorg. Nucl. Chem. Lett.*, 10, 301.
16. **Frisch MJ, (2009).** Gaussian 09.
17. **Becke Axel D. (1993).** A new mixing of Hartree–Fock and local density-functional theories. *Journal of Chemical Physics*, **98** 2 1372.
18. **Farghaly OA, Al–Saidi HM, Naggar AH, El–Mabrouk IM** (**2015)** Metal Complexes and Determination of Nalidixic Acid by Potentiometric and Conductometric Methods, *International Journal Of Electrochemical Science*, **12** 9865 – 9881
19. **Mishra M, Tiwari K, Mourya P, Singh MM, Singh VP (2015).** Synthesis, characterization, and corrosion inhibition property of nickel(II) and copper(II) complexes with some acyl hydrazine Schiff bases. *Polyhedron*, **89** 29–38.
20. **Chafaa S, Daoud D, Douadi T, Issaadi S** (**2014).** Corrigendum to ''Corrosion behavior of each phase in low carbon microalloyed ferrite–bainite dual-phase steel: Experiments and modeling'' *Corrosion Science*, **79** 50–58.
21. **Chan ECS, Krieg NR, Pelczar MJ (2001).**Textbook of Microbiology, 5thedi, *McGraw hill publishing company Ltd*., New Delhi, India.
22. **Mehrotra R., Shukla SN., Rai N., Gaur P (2019).** Systematic evaluation of lipophilicity in correlation with pharmacophore identification to develop potent bacterial inhibitors, *Chemistry Africa*, 2625-634.
23. **Mir, JM, Maurya RC, Vishwakarma PK (2017).** Corrosion resistance and thermal behavior of acetylacetonato-oxoperoxomolybdenum(VI) complex of maltol: Experimental and DFT studies. *Karbala International Journal of Modern Science*, **3 4** 212–223.
24. **Takjoo, R, Mague JT, Akbari A, Ahmadi M (2013)** Synthesis, spectral, DFT and X-ray study of a cis-MoO_2 complex with a new isothiosemicarbazone ligand, *Journal of Coordination Chemistry, **66** 11 1854–1865*.
25. **Mirsattari SN, Rajaei I (2015),** Synthesis and spectroscopic properties of a W(VI) binuclear complex of a novel tetradentate asymmetrical Schiff base ligand and its DFT study, *Polyhedron*, **102** 479-489.

26. **Asha, TM, Kurup MRP (2018).** Synthesis, spectroscopy, electrochemistry, crystal structures, and in vitro cytotoxicity of mononuclear molybdenum(VI) complexes incorporating tridentate ONO donor aroylhydrazone with auxiliary coordination site. *Inorganica Chimica Acta,* **483** *44–52.*
27. **Maurya R C, Pandey A, Sutradhar D** (**2004).** Synthesis magnetic and spectral studies of some novel binuclear dioxomolybdenum(VI)chelates involving Schiff bases derived from sulpha drugs and 4-benzoyl-3-methel-1-phenyl-2-pyrazolin-5-one, *Indian Journal Of Chemistry,* **43** 763-768.
28. **Holm RH, Sung KM, (1999).** Synthesis and structures of bis(dithio-lene)-tungsten(IV) complexes related to the active sites of tungs-toenzymes. *Inorganic Chemistry,* **39** 6 1275–1281.
29. **Alírio R, Filipe AP, Isabel G, Martyn P, Marta A, Sandra G, Tatiana A (2009).** Microwave-Assisted Synthesis and Crystal Structure of Oxo(diperoxo)(4,4'-di-tert-butyl-2,2'-bipyridine)-molybdenum(VI). *Molecules,* **14** 9 3610–3620.
30. **Maurya, RC, Vishwakarma PK, Mir JM, Rajak DK (2016).** Oxidoperoxidomolybdenum(VI) complexes involving 4-formyl-3-methyl-1-phenyl-2-pyrazoline-5-one and some β-diketoenolates. *Journal of Thermal Analysis and Calorimetry,* **124** 1 57–70.
31. **Glowiak T, Sobczak JM, Ziolkowski JJ (2003).** The structure of binuclear Molybdenum (VI) oxocomplexes with dianonic tridentate Schiff bases. *Applied Catalysis A: General,* **248** 261–268.
32. **Panhwar, QK, Shahabuddin M (2014).** Synthesis of Cr(III)-Morin Complex: Characterization and Antioxidant Study. *The Scientific World Journal, 1–8.*
33. **Bohre P, Maurya RC, Sutradhar D, Sahu S**, **(2008).** Synthesis, Characterization And 3d Molecular Modeling Of Some New 8-Coordinate Cis-Dioxomolybdenum Vi) Chelates Involving (O, N, O)- Donor Coordination Matrix Of Schiff Bases Derived From 4-Amino-2,3-Dimethyl-1-Phenyl-2-Pyrazolin-5-One And Some B–Diketoenolates, *Rasayan J. Chem,***1** 2 395-412.
34. **Litos G, Triantafyllidis G, Zabulis X (2006).** Synchronous Image Acquisition based on Network Synchronization, *Proceedings of the 2006 Conference on Computer Vision and Pattern Recognition Workshop (CVPRW'06)* **ISBN:** 0-7695-2646-2
35. **Maurya RC, Bohre P, Sahu S, Martin MH, Sharma AK, Vishwakarma P (2011).** Oxoperoxomolybdenum(VI) complexes of catalytic and biomedical relevance: Synthesis, characterization, antibacterial activity, and 3D-molecular modeling of some oxoperoxomolybdenum(VI) chelates in mixed (O, O) coordination environment involving maltol and β-diketoenolates. *Arabian Journal of Chemistry,* **9** 150–160.
36. **Dave RH, Kuddushi WMY, Patidar VL, Patel MS, Patel RK, Malek WAH (2018).** Synthesis And Characterization Of Schiff Base Aniline With 5-Bromo -2- Hydroxyl Benzaldehyde And Their Metal Complexes, *International Journal of Recent Scientific Research,* **9** 4 26026-26030.
37. **Abdulghani AJ, Hussain RK (2015).** Synthesis and Characterization of Schiff Base Metal Complexes Derived from Cefotaxime with ^{1}H-indole-2,3-dione (Isatin) and 4-N, N-dimethyl-amino benzaldehyde, *Journal of Inorganic Chemistry,* **5** 83-101.
38. **Boghaei DM, Mohebi S (2002).** Non-symmetrical tetradentate vanadyl Schiff base complexes derived from 1,2-phenylene diamine and 1,3-naphthalene diamine as catalysts for the oxidation of cyclohexene, *Tetrahedron,* **58** 5357-5366.
39. **Foris A**, **(2000).** 47,49 Ti and 13 C NMR spectra of titanium-containing catalysts, *Magnetic Resonance In Chemistry,* **38** 1044–1046
40. **Singh C P, Rao D P, Gautam R K, (2022).** Cis-Dioxomolybdenum (VI) Complexes with N-donor Macrocyclic Ligands, *Biointerface Research In Applied Chemistry,* **121** 1352 – 1364.